This article has been accepted for publication in a future issue of this journal, but has not been fully edited. Content may change prior to final publication. Citation information: DOI 10.1109/TMI.2019.2932014, IEEE Transactions on Medical Imaging

Dynamic *in vivo* X-ray Fluorescence Imaging of Gold in Living Mice Exposed to Gold Nanoparticles

Seongmoon Jung, Taeyun Kim, Wooseung Lee, Hyejin Kim, Hyun Suk Kim, Hyung-Jun Im, and Sung-Joon Ye*

***Abstract*—Dynamic *in vivo* biodistribution of gold nanoparticles (GNPs) in living mice was first successfully acquired by a pinhole X-ray fluorescence (XRF) imaging system using polychromatic X-rays. The system consisted of fan-beam X-rays to stimulate GNPs and a 2D cadmium zinc telluride (CZT) gamma camera to collect K-shell XRF photons emitted from the GNPs. 2D XRF images of kidney slices of three Balb/C mice were obtained within 2 minutes of irradiation per slice. 40 mg of GNPs suspended in a 0.2 mL phosphate-buffered saline was injected into the mice via a tail vein. The mice were scanned over a 60 min period after the injection of GNPs in order to acquire a dynamic biodistribution of GNPs. The concentrations of GNPs measured by the CZT gamma camera were then validated by inductively coupled plasma atomic emission spectroscopy and *ex vivo* L-shell XRF measurements using a silicon drift detector. The GNP concentrations in the right-side kidneys were 1.58% by weight (wt%) at T=0 min and 0.77 wt% at T=60 min after the injection. This investigation showed a dramatically reduced scan time and imaging dose. Hence, we conclude that dynamic *in vivo* XRF imaging of GNPs is technically feasible in a benchtop system. The developed pinhole XRF imaging system can be a potential molecular imaging modality for metal nanoparticles to emerge as a radiosensitizer and a drug-delivery agent.**

***Index Terms*—X-ray Fluorescence, Pinhole, Gold nanoparticles, in vivo, Molecular imaging**

I. Introduction

Preclinical studies using gold nanoparticles (GNP) injected into small animals indicate that the dynamic biodistribution of GNPs is crucial to evaluating biological effect and toxicity [1, 2]. The most common method used for this purpose is to measure the *ex vivo* concentration of GNPs using inductively coupled plasma-mass spectroscopy (ICP-MS), or -atomic emission spectroscopy (ICP-AES) and graphite furnace atomic absorption spectrometry (GFAA) [1, 3]. Although these methods measure very low concentrations of GNPs (i.e., in ppb), they require complex sampling procedures such as tissue excision, freeze-drying, and chemical preprocessing.

In preclinical studies, modalities such as optical fluorescence imaging, diffuse optical tomography, and photo-acoustic imaging have been widely used to measure *in vivo* biodistributions of GNPs [1, 4-6]. However, those modalities have a substantial limitation on imaging depth due to light scattering [7]. Recently, with the technical advance of energy resolving detectors, *in vivo* imaging of high atomic number (Z) metal nanoparticles using a spectral CT has also been studied [8]. In addition to the aforementioned molecular imaging modalities, another promising method is X-ray fluorescence (XRF) imaging or X-ray fluorescence computed tomography (XFCT) [1, 2, 9]. In the early stage of XFCT studies, the experiments were performed using monochromatic X-rays from synchrotron facilities [10]. However, due to the limited access to synchrotron facilities, researchers utilized polychromatic X-ray sources that are now available on a laboratory scale [11]. In 2016, Cho's research group reported a study, wherein 1.9 nm diameter GNPs were injected into a mouse, and later imaged postmortem using a benchtop XFCT system [7]. Since their XFCT system used a single-pixel cadmium telluride (CdTe) detector with a parallel hole collimator, the image acquisition time was about 90 min per slice. More recently, a benchtop XFCT system with a linear-array cadmium zinc telluride (CZT) detector was developed for *in vivo* imaging of gadolinium in living mice exposed to gadolinium nanoparticles [12]. With an implementation of the linear-array detector, the image acquisition time was reduced to 7.5 min per slice. Such a long scan time might not be suitable for *in vivo* measurement of biodistribution that has to be completed in a short period after the injection.

This work aims to show the experimental feasibility of dynamic *in vivo* XRF imaging of GNPs in living mice using polychromatic X-rays. By collecting K-shell XRF photons using a commercial 2D CZT gamma camera, the imaging system was expected to have a short image acquisition time and deliver a low imaging dose. By using a pinhole collimator, we can acquire a 2D slice image directly from a single sheet of fan-beam irradiation without image reconstruction or rotation of the object or detector [9]. Because XRF photons stimulated by incident X-rays are isotropic, XRF photons passing through the

Manuscript received July 8, 2019. This work was supported in part by the National Research Foundation of Korea (NRF) under Grant No. NRF-2013M2B2B1075776. *Asterisk indicates corresponding author*. S. Jung, T. Kim, W. Lee, H. Kim, H. S. Kim. H.-J. Im and S.-J. Ye* are in Biomedical Radiation Sciences, Department of Transdisciplinary Studies, Graduate School of Convergence Science and Technology, Seoul National University, Seoul 03087, Korea (e-mail: smjung@snu.ac.kr; mindpalace233@gmail.com, victolee@snu.ac.kr, hyejin0815@snu.ac.kr, goldsuk89@gmail.com, iiihjjj@snu.ac.kr and sye@snu.ac.kr).

This article has been accepted for publication in a future issue of this journal, but has not been fully edited. Content may change prior to final publication. Citation information: DOI 10.1109/TMI.2019.2932014, IEEE Transactions on Medical Imaging

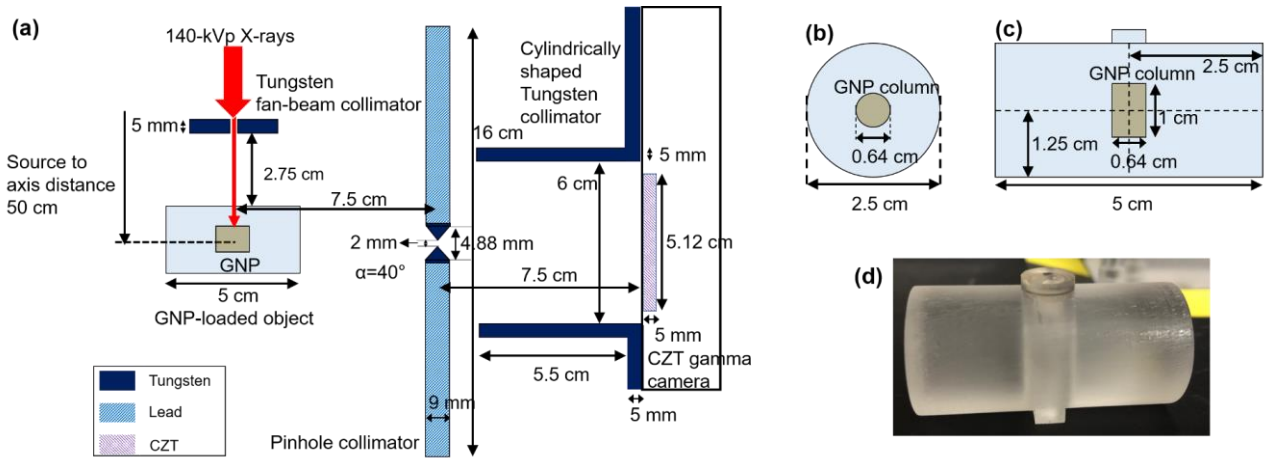

Fig. 1. (a) Schematic illustration of experimental setup of *in vivo* pinhole XRF imaging system consisting of a pinhole collimator, a tungsten collimator, and a CZT gamma camera. (b)-(c) top- and lateral-view of PMMA imaging phantom. (d) Photograph of PMMA imaging phantom.

pinhole to reach the position-sensitive CZT gamma camera have their own positions and energy information. The dynamic *in vivo* XRF imaging of GNPs in the kidneys of three Balb/C mice was performed. The concentrations of GNPs in the kidneys were quantified with respect to the time that had elapsed after the injection. Furthermore, this study also investigated the feasibility of using an L-shell XRF detection system with a silicon drift detector (SDD) to measure *ex vivo* GNP concentrations from excised biological samples. It would be advantageous over ICP-AES that requires the complex sampling procedures. The concentrations measured by the *in vivo* XRF imaging system and the L-shell *ex vivo* XRF detection system were cross-compared. The measured *ex vivo* concentrations were then validated by ICP-AES.

II. Methods

A. Pinhole X-ray Fluorescence Imaging System

The pinhole K-shell XRF imaging system consists of a tungsten fan-beam collimator, a pinhole collimator, a tungsten collimator, and the CZT gamma camera (Integrated Detect Electronics AS, Oslo, Norway). The pinhole collimator and the CZT gamma camera were placed perpendicular to a beam direction (Fig. 1(a)). The inner and the outer diameter of the pinhole were 2 mm and 4.88 mm, respectively, with an acceptance angle of 40°. The pinhole of the collimator was made of tungsten while the rest of the collimator was made of lead. The thickness of the entire collimator was 9 mm. The cylindrically shaped 5 mm thick tungsten collimator was attached to the front window of the CZT gamma camera to shield photons leaking from the X-ray tube. The inner diameter of the tungsten collimator was 6 cm. The X-ray source to axis distance was 50 cm, where the axis was defined as a line passing through the center of the pinhole and the CZT gamma camera. The beam plane-to-collimator and the collimator-to-detector distances were both 7.5 cm. A commercial CZT gamma camera composed of four SRE4001-CZT25.4 modules (Integrated Detect Electronics AS, Oslo, Norway) was used. The CZT gamma camera consisted of 32 × 32 pixels of which each pixel had a dimension of 1.6 × 1.6 mm^2 and a 5 mm thickness. The CZT gamma camera had an Al6061 window of 1.5 mm thickness in front of the CZT crystal. The detector had 100% detective quantum efficiency due to the high attenuation coefficient of CZT. The field of view of this system was 4.8 cm in diameter.

X-rays of 140-kVp generated by X-RAD 320 (X-RAD 320, Precision X-ray Inc., North Branford, CT, USA) were used as the excitation source. The current to the X-ray tube was determined to be 17 mA that did not exceed the maximum count rate for the CZT gamma camera. The maximum count rate was about 5.2×10^4 counts/sec for 1024 pixels. A tungsten fan-beam collimator with a 2 mm slit was used to generate a fan-beam having a thickness of 2.2 mm at a source to surface distance of 47.25 cm. The thickness of the fan-beam X-rays was measured by XR-RV3 radiochromic film at the surface of an imaging phantom. When the fan-beam X-rays interact with the GNP-loaded object, the secondary photons, including those from Compton scattering and XRF, pass through the pinhole to reach the CZT gamma camera.

A polymethyl methacrylate (PMMA) phantom of 2.5 cm diameter and 5 cm length was imaged to acquire a calibration curve to correlate GNP concentrations to XRF counts (Fig. 1(b)-(d)). In the phantom a 1.0 cm diameter hole was placed, where GNP columns having six different concentrations were inserted that were 0.0% by weight (wt%), 0.125 wt%, 0.25 wt%, 0.5 wt%, 1.0 wt%, and 2.0 wt%. 1.9 nm diameter GNPs (AuroVist, Nanoprobes Inc., NY, USA) were diluted with deionized water (DI water). The GNP column had an inner diameter of 0.64 cm and an outer diameter of 1.0 cm. The height of the GNP column was 1.0 cm. For the calibration, the phantom was irradiated for 1 min. The measurement was repeated ten times for each GNP concentration.

B. Image Processing

The CZT gamma camera could not measure two separate XRF peaks (67.2 keV for $K_{\alpha2}$, 69.0 keV for $K_{\alpha1}$) due to the limitation of the energy resolution of the detector. Instead, one K-shell XRF peak from GNPs is shown at the energy window

This article has been accepted for publication in a future issue of this journal, but has not been fully edited. Content may change prior to final publication. Citation information: DOI 10.1109/TMI.2019.2932014, IEEE Transactions on Medical Imaging

between 65.6 keV and 71.0 keV. The raw XRF signals were acquired by subtracting the photon counts of the XRF peak channels of the 0.0 wt% PMMA phantom from the counts of the same channels of the GNP-loaded PMMA phantom. The width of the channel windows was 4 channels (i.e., 5.4 keV in energy).

The correction factors were applied to raw XRF counts. We considered the attenuation of the incident X-rays as well as XRF photons emitted from GNPs. The method for the attenuation correction was the same as in our previous Monte Carlo (MC) study [9]. We additionally carried out a pixel-by-pixel non-uniformity correction of the raw XRF counts by measuring the photon counts of a uniform photon field produced by a Cd-109 radioisotope (Type R, Eckert & Ziegler). This non-uniformity might be due to a defect in the CZT crystal, a charge sharing effect, or electrical noise. The source to detector distance was 25 cm. Gamma rays emitted from Cd-109 were measured by the CZT gamma camera for 41 hours at room temperature. The photon counts measured by each pixel of the detector were normalized against the maximum counts among the pixels. The reciprocals of each value are the pixel-by-pixel non-uniformity correction factors. By multiplying all the correction factors by the raw XRF signals of each pixel, corrected XRF photon counts were obtained. A Gaussian filter was applied to decrease noise. The linear relationship between the GNP concentrations and the mean count number per pixel in the region of interest (ROI) was derived. The ROI was the pixels projected by the GNP columns. Since the projected area of the GNP columns on the CZT gamma camera was 0.64 × 1 cm^2, the ROI had 4 × 6 pixels (i.e., 0.64 × 0.96 cm^2).

C. L-shell XRF Detection System

For the measurement of *ex vivo* L-shell XRF photons, X-rays of 40-kVp generated by X-RAD 320 were used as the excitation source. The 40-kVp X-rays were filtered with Al 2 mm. The current to the tube was 10 mA and the incident X-rays of the square radiation field fully covered the samples. The SDD (X-123SDD, Amptek, USA) was perpendicular to the beam direction (Fig. 2). The front window of SDD was located 3.0 cm from the center of the sample. The peaking time of the detector was 3.2 μs. Under this measurement setup, the SDD had an energy resolution in the range of 0.135-0.140 keV full width half maximum at 5.9 keV, while the maximum count rate was expected to fall in the range from 1 × 10^5 to 2 × 10^5 counts/sec according to the specifications provided by the manufacturer.

We measured L-shell XRF photons from 0.0078 wt%, 0.0313 wt%, 0.125 wt%, 0.25 wt%, 0.5 wt% and 1.0 wt% of GNPs stirred into 30 mg of DI water. The samples for calibration had an inner diameter of 5 mm and an outer diameter of 8 mm. The irradiation time was 5 min for each sample. The relationship between the GNP concentrations and the L-shell XRF counts was obtained. The measurement was repeated five times for each GNP sample. A sum of the two L-shell XRF peaks was used to create a calibration curve. The most dominant two peaks were the $L_{\alpha 1}$ XRF peak of 9.71 keV and the $L_{\beta 1}$ XRF peak of 11.48 keV. In order to generate a background curve for discriminating the $L_{\alpha 1}$ XRF peak, data points from the off-peak

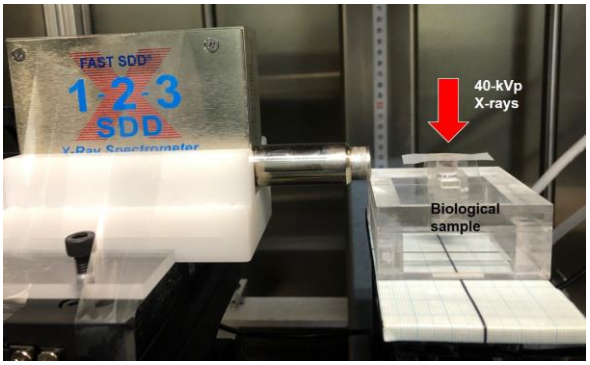

Fig. 2. Photograph of L-shell XRF detection system for a measurement of *ex vivo* concentrations of GNPs in biological samples.

ranges of 9.08-9.32 keV, and 9.96-10.10 keV were selected. By using a linear interpolation, the background curve was acquired under the $L_{\alpha 1}$ XRF peak. The $L_{\beta 1}$ XRF peak from the GNPs was allowed to overlap with K_α XRF peak of bromine (Br). This peak might have been generated from the head material of SDD. For the discrimination of the $L_{\beta 1}$ XRF peak, a Gaussian function was applied to mimic the shape of the K_α XRF peak of Br. Pure $L_{\beta 1}$ XRF counts from GNPs were extracted by subtracting generated the Gaussian background curve from the overlapped $L_{\beta 1}$ XRF peak.

D. Mice Study

The three mice were 6 week old female Balb/C, weighing 15-17 g ($n = 3$). All experiments were conducted in accordance with the protocols and guidelines approved by the Seoul National University Institutional Animal Care and Use Committee. 1.9 nm diameter GNPs (AuroVist, Nanoprobes Inc., NY, USA) were prepared according to the instruction provided by the manufacturer. The 40 mg of GNPs was suspended in 0.2 mL phosphate-buffered saline solution. The mice were anesthetized with isoflurane gas via inhalation for about an hour. They were restrained in a prone position and three slices for each mouse were set to the light field of the fan-beam of X-RAD 320 as shown in Fig. 3. Before the injection of the GNP-containing solution, pre-scanning of each mouse was performed for 1 min for each slice. The thickness of the slice was 2 mm. Following the pre-scanning, the GNP-containing solution was injected into the mice via a tail vein. Subsequent to the injection of GNP-containing solution, the mice were scanned at T = 0, 10, 20, 30, 45, and 60 min. At every time point, the post-scanning was performed for 1 min for each slice.

After T = 60 min, the mice were euthanized via CO_2 inhalation and then we extracted the left and right kidneys, spleen, liver, and blood from the three mice. The total number of tissue samples was 15, while 3 organs of each type listed above were extracted. The extracted organs were then excised into small pieces whose diameters were less than 3 mm so that could measure L-shell XRF from those samples. The L-shell detection system with X-rays of 40-kVp was used to measure L-shell XRF photons emitted from the samples. The irradiation time was 5 min for each sample. ICP-AES (OPTIMA 8300, Perkin-Elmer, USA) was again used to measure the mass of GNPs within the same excised organs.

This article has been accepted for publication in a future issue of this journal, but has not been fully edited. Content may change prior to final publication. Citation information: DOI 10.1109/TMI.2019.2932014, IEEE Transactions on Medical Imaging

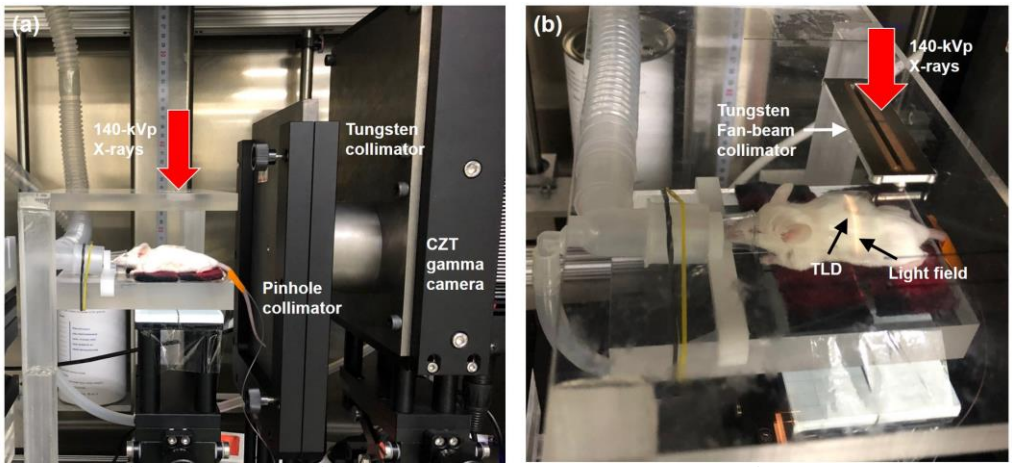

Fig. 3. (a) Schematic illustration of experimental setup of *in vivo* pinhole XRF imaging system consisting of a pinhole collimator, a tungsten collimator, and a CZT gamma camera. (b)-(c) top- and lateral-view of PMMA imaging phantom. (d) Photograph of PMMA imaging phantom.

E. Radiation Dose

In order to measure the radiation dose delivered to the skin of the mice during the imaging interval, TLD-100 detectors (Harshaw, Thermo Fisher Scientific, denoted as TLD) were used. TLDs were calibrated by filtered 140-kVp of X-RAD 320. The reference dosimetry was performed by following the TG-61 in-air measurement protocol with a 0.6cc farmer-type ion chamber (30013, PTW, Germany) and electrometer (PTW, Germany) [13]. TLDs were attached to the skin of the mice where indicated by a light field (Fig. 3(b)). After the irradiation, TLDs were read out by TLD Reader (Harshaw 3500, Thermo Fisher Scientific).

III. Results

A. Pinhole X-ray Fluorescence Imaging system

Fig. 4 shows the XRF images of 0.125 wt%-2.0 wt% GNP-loaded PMMA phantom. The corrected XRF photon counts in the ROIs increased as the concentration of GNPs increased. Under this imaging setup, 0.125 wt% of GNPs could be detected. The calibration curve between the GNP concentrations and the mean count number per pixel of ROI was obtained by using the GNP-loaded PMMA phantom (Fig. 5). It shows a good linear relationship (i.e., R^2=0.9993).

Fig. 6 shows the measured spectra of K-shell XRF and Compton scattered photons from the right kidney of mouse 1 (denoted as M1) at pre-injection, and post-injection at T = 0, 30, 60 min. When compared with the measured spectrum at pre-injection, clear Au K_α XRF peaks within the energy window (vertical dashed lines in Fig. 6) were observed in those spectra measured post-injection. The raw XRF counts were obtained by subtracting the photon counts at pre-injection from the photon counts at post-injections within the energy window. These raw XRF counts were then treated for the attenuation, the sensitivity, the pixel-by-pixel non-uniformity corrections, and the Gaussian filter.

Fig. 7 shows the XRF images of M1 at post injection T = 0, 10, 30, 60 min and XRF images fused with Compton scattered photon image. The image of Compton scattered photons could at least provide a structure of the surface of the mice body. At T = 0 min, the maximum concentration of GNPs in the right kidney of M1 was observed. After T = 10 min, the GNPs in the right kidney of M1 were excreted and a pair of kidneys was shown in the XRF images.

Fig. 8 shows XRF images of mouse 2 (denoted as M2) and mouse 3 (denoted as M3) at post injection T = 0 min and Compton/XRF fusion images. The right kidneys were observed in both XRF images. Although we measured two more slices in the superior direction for each mouse, the left kidneys were not observed. The left kidney might be located in different slices in the inferior direction. Therefore, clearance data of GNPs in the right kidneys from three mice ($n = 3$) were obtained over a 60 min period (Fig. 9). The concentration of GNPs at T = 60 min was decreased by half from the concentration at T = 0 min. This tendency of GNPs in the kidneys to reduce in concentration

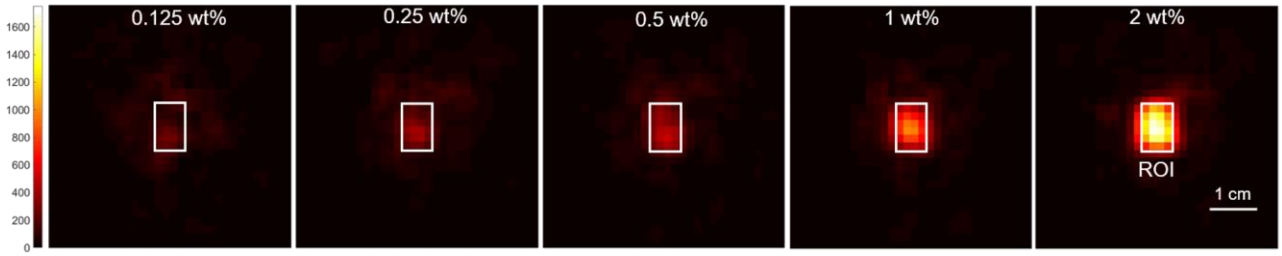

Fig. 4. XRF images of 0.125 wt%-2.0 wt% GNP column-loaded PMMA phantom. The images were randomly selected from ten measurements for each GNP concentration. The white rectangle indicates the ROI (i.e., 4 × 6 pixels). The colorbar indicates photon counts multiplied by the correction factors.

This article has been accepted for publication in a future issue of this journal, but has not been fully edited. Content may change prior to final publication. Citation information: DOI 10.1109/TMI.2019.2932014, IEEE Transactions on Medical Imaging

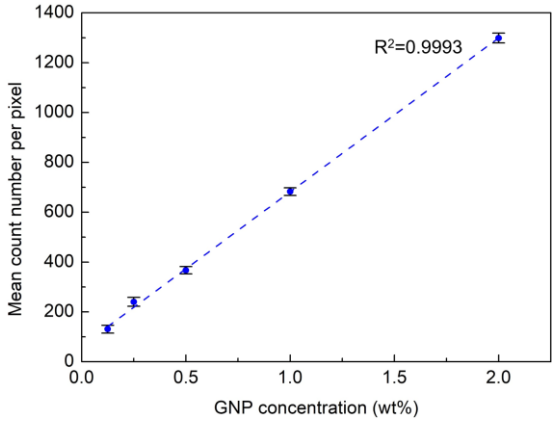

Fig. 5. Linear relationship between GNP concentrations and corrected mean count number per pixel measured by the CZT gamma camera. Dashed line indicates a linear regression curve. Error bars for data points are similar to the size of the data symbols.

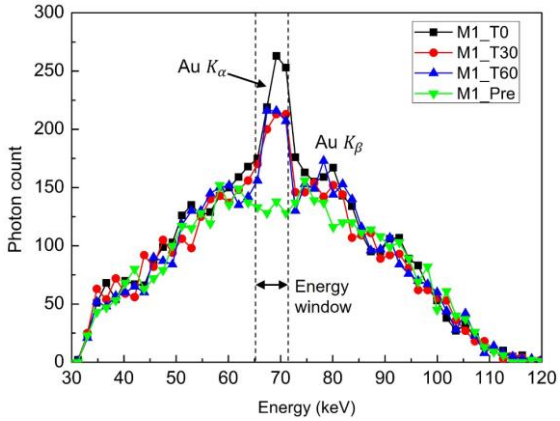

Fig. 6. Measured spectra of K-shell XRF of GNPs and Compton scattered photons from a right kidney of mouse 1 (M1) at pre-injection (pre), post-injections T=0 min (T0), T=30 min (T30) and T=60 min. (T60).

with increasing T was comparable with the results from previous studies [3, 14].

B. L-shell XRF Detection System

Fig. 10 shows the measured energy spectrum for 0.125 wt% GNPs and their background curves generated for discrimination of the $L_{\alpha 1}$ XRF peak and $L_{\beta 1}$ XRF peak. A calibration curve between the GNP concentration and L-shell XRF count was obtained by using the L-shell XRF detection system (Fig. 11). Because the L-shell XRF photons emitted from the high concentrations of GNP suffered from self-absorption in the samples, the relationship between the measured L-shell XRF photons and the concentrations of GNP was assumed to follow an exponential function (i.e., R^2=0.9917) rather than a linear function. Under this measurement setup, 0.0078 wt% GNPs could be detected.

Fig. 12 shows the measured spectra of the L-shell XRF of GNPs in the excised organs from the euthanized M3, and K-shell XRF photons from the head of the detector. In comparison with the measured spectra from the blood, liver, and spleen, higher photon counts of Au L_α and L_β XRF peaks were observed in the spectra measured from a pair of kidneys. The concentrations of GNPs in the excised organs of the three mice were estimated by the calibration curve shown in Fig. 11. Fig. 13 illustrates the GNP concentrations in the organs harvested

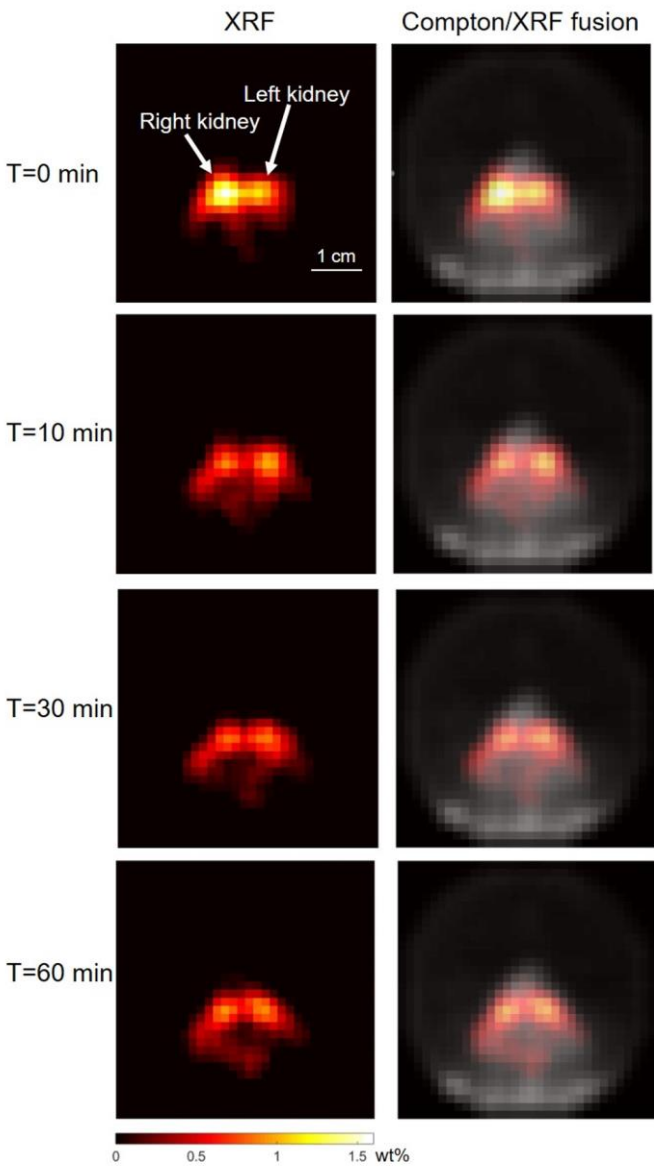

Fig. 7. Left column shows XRF images of kidneys of mouse 1 (M1) at post-injection T=0, 10, 30, 60 min. The right column shows XRF images fused with the Compton scattered image acquired at pre-injection. The white arrows indicate the location of kidneys.

from the euthanized mice (n = 3). The concentrations measured by the L-shell XRF detection system were validated with the concentrations measured by ICP-AES. The difference in GNP concentrations of both kidneys measured by the L-shell XRF detection system and ICP-AES was 0.05-0.08 wt%.

This article has been accepted for publication in a future issue of this journal, but has not been fully edited. Content may change prior to final publication. Citation information: DOI 10.1109/TMI.2019.2932014, IEEE Transactions on Medical Imaging

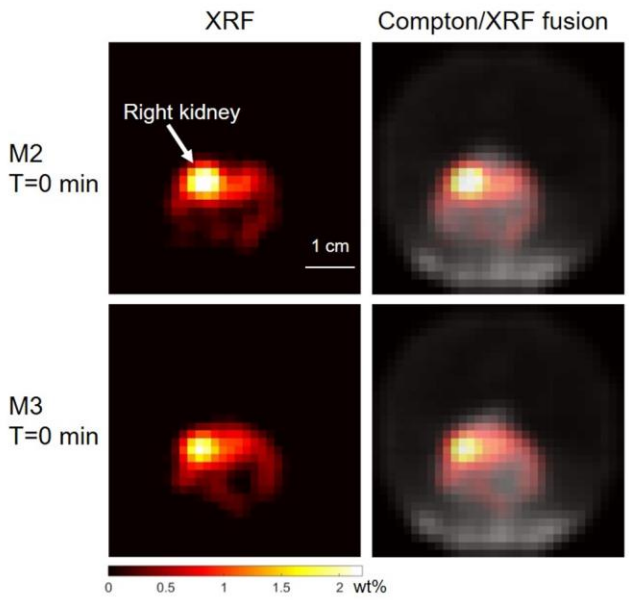

Fig. 8. Left column shows XRF images of kidneys of mouse 2 (M2, top) and mouse 3 (M2, bottom) at post-injection T=0 min. Right column shows XRF images fused with Compton scattered images acquired at pre-injection; top: M2 and bottom: M3. The white arrow indicates the location of right kidney.

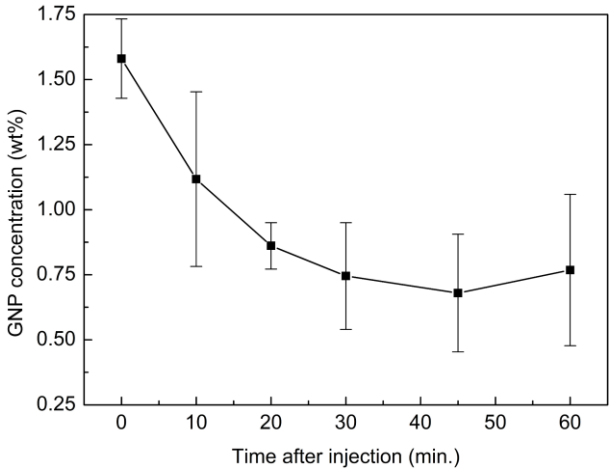

Fig. 9. Clearance of GNPs showing biodistributions in mice right kidneys (n=3) over a 60 min period after 40 mg of GNP injection.

C. Radiation Dose

The radiation doses to the skin of the three mice measured by TLDs are listed in Table I. The average dose was 107 mGy during the acquisition of one slice image (i.e., the sum of the pre-scan (1 min) and the post-scan (1 min)). Using the system, we have developed, the total dose during the full *in vivo* imaging period was expected to be about 1120 mGy.

IV. Discussion

The developed system using filtered 140-kVp X-rays could detect GNP columns as low as 0.125 wt%. The system acquired 2D XRF images directly from a pre- and post-scan of fan-beam irradiations without any further process of translation and rotation of objects so that a short image acquisition time (i.e., 2 min for one image slice) could be achieved. The clearance data

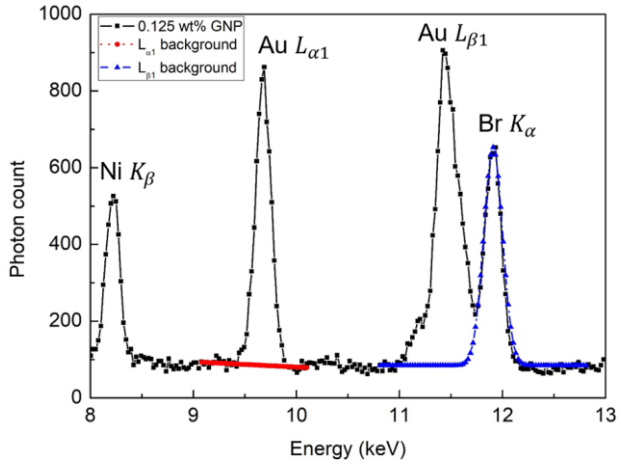

Fig. 10. The energy spectrum measured for 0.125 wt% GNPs (black solid line). The background curves generated for discrimination of $L_{\alpha 1}$ and $L_{\beta 1}$ XRF peaks are indicated as a red dotted line with circles and a blue dash-dot line with triangles, respectively.

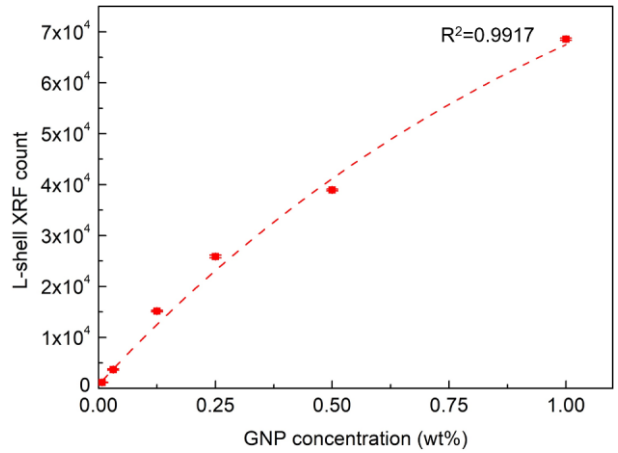

Fig. 11. Exponential relationship between GNP concentration and L-shell XRF count measured by SDD. Dashed line indicates an exponential fitting curve. Error bars for data points are much smaller than the size of the data symbols.

of kidneys of the three mice were acquired from the XRF images. By measuring the L-shell XRF photons from excised organs, the L-shell detection system estimated much lower concentrations of GNPs than did the *in vivo* XRF imaging system. This was validated by ICP-AES. In particular, the GNP concentration of the right kidneys measured by *in vivo* XRF images at T = 60 min after the injection was about 0.19-0.23 wt% lower than those concentrations analyzed by *ex vivo* measurements. This might be due to the heterogeneous distribution of gold in kidney. In order to avoid such discrepancies, it would be better to compare the concentrations of kidney homogenate samples. The concentrations of GNP in

TABLE I
SKIN DOSE MEASURED BY TLDS

Mouse	Total dose (mGy)	Dose/image slice (mGy)
1	1075	102
2	1120	107
3	1166	111
Average	1120±37	107±4

This article has been accepted for publication in a future issue of this journal, but has not been fully edited. Content may change prior to final publication. Citation information: DOI 10.1109/TMI.2019.2932014, IEEE Transactions on Medical Imaging

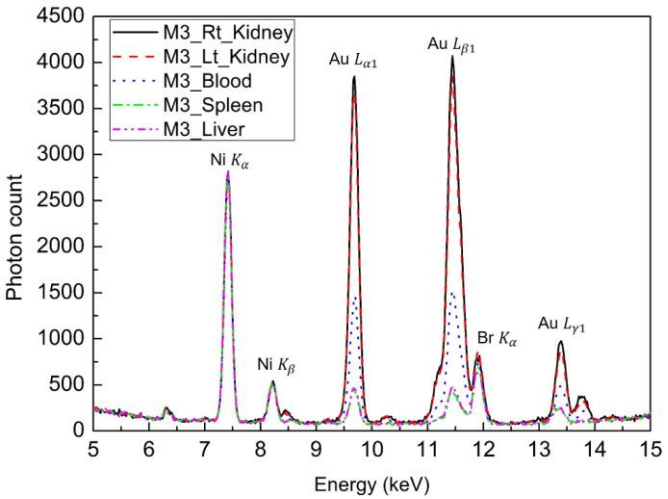

Fig. 12. The energy spectra measured for right kidney (Rt_Kidney), left kidney (Lt_Kidney), blood, spleen and liver excised from mouse 3 (M3) after euthanasia.

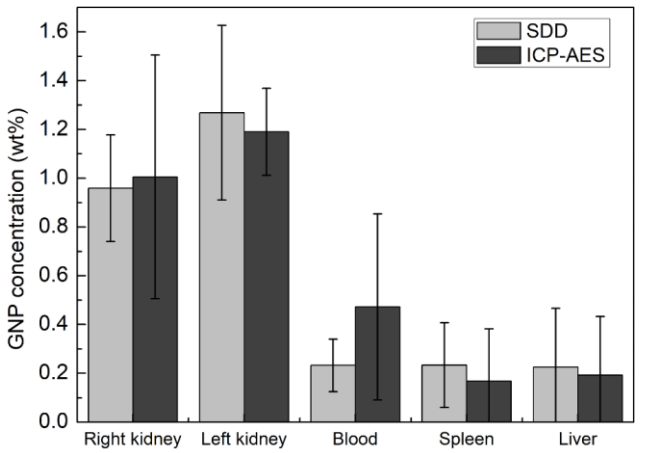

Fig. 13. GNP concentration in organs harvested from three mice 60 min after injection. Concentration is measured with both L-shell XRF detection system (SDD) and ICP-AES. Error bars indicate standard deviations at 95% confidence level.

kidneys with normal function decayed exponentially as presented by Xu *et al* [14]. In fact, the concentrations in kidneys over 15 min after the injection could exhibit fluctuations and may display mouse-to-mouse variations [14].

The relationship between the L-shell XRF counts and the GNP concentrations should be linear when the self-absorption of L-shell XRF counts in the sample is corrected. As reported by Ricketts *et al.* [15, 16] and Manohar *et al.* [17], the self-absorption in the sample could be corrected by dividing the measured L-shell XRF counts by the Compton scattered photon counts. In order to implement the scatter-correction technique, a parallel hole collimator is required to be additionally configured into our L-shell XRF detection system in future work.

The concentrations of GNPs accumulated in the organs or tumors in mice depend on the injected dose of GNPs and the characteristics of GNPs (e.g., size, shape and surface-coating). This is particularly true, in the previous studies conducted by Hainfeld *et al.* [3] and Manohar *et al.* [7], that used the same 1.9 nm diameter GNPs without surface-coating (i.e., passive targeting) as used in this study, where 40-54 mg of GNPs had been injected into the mice [3, 7]. Although, such an injected dose is still acceptable in terms of LD_{50} (i.e., 2.7 g Au/kg) [3], the injected dose in the aforementioned studies was much higher than the dose for typical *in vivo* studies using GNPs. In order to use this XRF imaging technique as a preclinical molecular imaging modality, the XRF imaging system should be improved to detect the GNP concentrations as low as an order of 0.001 wt% (i.e., a few ppm level) [15-17]. The detectable concentration is dependent on the performance (i.e., the energy resolution and maximum count rate) of a detector. In early MC studies, it was assumed that the pixelated detectors have the same performance in terms of the energy resolution and maximum count rate as do single-pixel detector (e.g., X-123 CdTe or HPGe detector) [18, 19]. However, by overlooking an electronic noise, a charge sharing effect and a hole-tailing effect, those MC studies might have overestimated the image quality and detection limit. Therefore, some research groups have tried to develop pixelated detectors having a superior energy resolution and maximum count rate to enhance the detection limit of XFCT [20]. On the other hand, the characteristics (i.e., spectrum, intensity) of incident X-rays can also affect the detection limit significantly. Quasi-monochromatic X-ray spectra with sufficient intensity can be obtained by adopting a carbon nantobue X-ray source or an X-ray source using highly oriented pyrolytic graphite [21]. The implementation of such X-ray sources can improve the detection limit by increasing the XRF photon counts and decreasing the Compton scattered photons.

The radiation dose (~107 mGy) measured by TLDs during the image acquisition for one slice of a 2D image was similar to the imaging dose delivered by micro-CT (a few 100 mGy [22] and 260 mGy [23]). On the other hand, it was much lower than the imaging doses (610 mGy [12] and 743 mGy [7]) delivered by the XFCT systems used in the recent *in vivo* studies. However, the comparison was made between the systems at different system resolutions and slice thicknesses. For example, the system resolution of XFCT system developed by Cho's research group could vary with different step sizes and projection angles for data acquisition [7]. The system resolution of their system might have been above 2.5 mm, considering the diameter of the parallel hole of their collimator (i.e., 2.5 mm diameter) [7].

The system resolution of our imaging system (i.e., 4.4 mm) was quite large for the size of the small organs we investigated [24]. Hence, a magnification of the image by adjusting the distances between the beam plane-to-pinhole and pinhole-to-CZT gamma camera could be considered in future studies. For example, within a space available in our system (i.e., 15 cm), the magnification factor can be increased by 2 when the distances of the beam plane-to-pinhole and of the pinhole-to-CZT gamma camera are 5 cm and 10 cm, respectively. According the theoretical equations to calculate the system resolution [24], the increased magnification factor might improve the system resolution, i.e., from 4.4 mm to 3.4 mm. Furthermore, the use of a detector with smaller pixels and the

use of a smaller pinhole can be pursued to enhance the system resolution. With a pinhole of 1 mm diameter, a 2.6 mm system resolution can be achievable. However, such an implementation will require increasing imaging time as well as an increased imaging dose.

Because a CT scan was not available in this study, anatomical information was not available. With the animal CT images, more accurate attenuation corrections for incident X-rays and XRF photons could be applied to estimate the biodistributions of GNP. Further, the XRF image fused with the CT images would be useful in preclinical practices. Other metal nanoparticles rather than GNP can be used as an agent for the XRF imaging system. Since the minimum detectable energy for the CZT gamma camera of our system is ~35 keV, the K-shell XRF from the metal nanoparticle whose atomic number is greater than 63 (i.e., ~41 keV for Eu) is measurable. In fact, we obtained the K-shell XRF images of Eu nanoparticles (not included in this manuscript). Thus, our XRF imaging system can be used to obtain the XRF images of multi-element metal nanoparticles injected into small animals in future studies.

V. Conclusions

A dynamic *in vivo* XRF imaging system and an *ex vivo* L-shell XRF detection system were successfully developed. The biodistribution of GNPs in mice measured by both systems was cross-compared and validated by ICP-AES. Using a 2D CZT gamma camera, dynamic *in vivo* XRF images were acquired and the image acquisition time was dramatically reduced to 2 min for one image slice. The system could provide potential *in vivo* molecular imaging modality for metal nanoparticles to emerge as a radiosensitizer and a drug-delivery agent. In the future, with the system combined with transmission X-ray imaging detectors, it will provide the anatomical information as well as the molecular information.

References

[1] J. Schuemann, R. Berbeco, D. B. Chithrani, S. H. Cho, R. Kumar, *et al*,. "Roadmap to Clinical Use of Gold Nanoparticles for Radiation Sensitization," *Int J Radiat Oncol*, vol. 94, pp. 189-205, Jan 1 2016.

[2] S. H. Cho and S. Krishnan, *Cancer nanotechnology: principles and applications in radiation oncology*, Boca Raton, FL: CRC Press, 2013, pp. 99-108.

[3] J. F. Hainfeld, D. N. Slatkin, T. M. Focella and H. M. Smilowitz, "Gold nanoparticles: a new X-ray contrast agent," *The British Journal of Radiology*, vol. 79, pp. 248-53, Mar 2006.

[4] L. Y. Chou and W. C. Chan, "Fluorescence-tagged gold nanoparticles for rapidly characterizing the size dependent biodistribution in tumor model," *Adv Healthc Mater*, vol. 1, pp. 714-21, Nov 2012.

[5] A. De La Zerda, C. Zavaleta, S. Keren, S. Vaithilingam, S. Bodapati, *et al.*, "Carbon nanotubes as photoacoustic molecular imaging agents in living mice," *Nat Nanotechnol*, vol. 3, pp. 557-62, Aug 2008.

[6] W. Li and X. Chen, "Gold nanoparticles for photoacoustic imaging," *Nanomedicine (Lond)*, vol. 10, pp. 299-320, Jan 2015.

[7] N. Manohar, F. J. Reynoso, P. Diagaradjane, S. Krishnan and S. H. Cho, "Quantitative imaging of gold nanoparticle distribution in a tumor-bearing mouse using benchtop X-ray fluorescence computed tomography," *Sci Rep*, vol. 6, p. 22079, 2016.

[8] S. Si-Mohamed, D. P. Cormode, D. Bar-Ness, M. Sigovan, P. C. Naha, *et al.*, "Evaluation of spectral photon counting computed tomography K-edge imaging for determination of gold nanoparticle biodistribution in vivo," *Nanoscale*, pp. 18246-257, 2017.

[9] S. Jung, W. Sung and S.-J. Ye, "Pinhole X-ray fluorescence imaging of gadolinium and gold nanoparticles using polychromatic X-rays: a Monte Carlo study," *Int J Nanomedicine*, vol. 12, pp. 5805-17, Aug 2017.

[10] P. Boisseau, "Determination of three dimensional trace element distributions by the use of monochromatic X-ray microbeams," Ph.D. dissertation, Dept. Phys., Massachusetts Inst. Technol., Cambridge, MA, 1986.

[11] S. K. Cheong, B. L. Jones, A. K. Siddiqi, F. Liu, N. Manohar, and S. H. Cho, "X-ray fluorescence computed tomography (XFCT) imaging of gold nanoparticle-loaded objects using 110 kVp X-rays," *Phys Med Biol*, vol. 55, pp. 647-62, Feb 7 2010.

[12] S. Zhang, L. Li, J. Chen, Z. Chen, W. Zhang and H. Lu, "Quantitative imaging of Gd nanoparticles in mice using benchtop cone-beam X-ray fluorescence computed tomography system," *Int J Mol Sci*, vol. 20, p.2315, May 2019.

[13] C.-M. Ma, C.W. Coffey, L. A. DeWerd, C. Liu, R. Nath, *et al.*, "AAPM protocol for 40-300 kV x-ray beam dosimetry in radiotherapy and radiobiology," *Med Phys*, vol. 28, pp.868-93, Jun 2001.

[14] J. Xu, M. Yu, P. Carter, E. Hernandez, A. Dang, P. Kapur, et al, "In vivo x-ray imaging of transport of renal clearable gold nanoparticles in the kidneys," *Angewandte Chemie*, vol. 56, pp. 13356-60, Oct 2017.

[15] K. Ricketts, A. Castoldi, C. Guazzoni, C. Ozkan, C. Christodoulou, *et al.*, "A quantitative x-ray detection system for gold nanoparticle tumor biomarkers," *Phys Med Biol*, vol. 57, pp. 5543-55, Aug 2012.

[16] K. Ricketts, C. Guazzoni, A. Castoldi, A. P. Gibson, and G. J. Royle, "An x-ray fluorescence imaging system for gold nanoparticle detection," *Phys Med Biol*, vol. 58, pp. 7841-55, Oct 2013.

[17] N. Manohar, F. J. Reynoso, and S. H. Cho, "Experimental demonstration of direct L-shell x-ray fluorescence imaging of gold nanoparticles using a benchtop x-ray source," *Med Phys*, vol. 40, pp.080702, Jul 2013.

[18] B. L. Jones and S. H. Cho, "The feasibility of polychromatic cone-beam x-ray fluorescence computed tomography (XFCT) imaging of gold nanoparticle-loaded objects: a Monte Carlo study," *Phys Med Biol*, vol. 56, pp. 3719-30, May 2011.

[19] C. A. S. Dunning and M. Bazalova-Carter, "Optimization of a table-top x-ray fluorescence computed tomography (XFCT) system," *Phys Med Biol*, vol. 63, pp. 235013, Nov 2018.

[20] M. Li, J. George and L.-J. Meng, "Broadband X-ray fluorescence emission tomography with a small pixel CdTe imaging-spectrometry detector," *J Nucl Med*, vol. 58, pp. 401, May 2017.

[21] N. Manohar, B. L. Jones and S. H. Cho, "Improving x-ray fluorescence signal for benchtop polychromatic cone-beam x-ray fluorescence computed tomography by incident x-ray spectrum optimization: A Monte Carlo study," *Med Phys*, vol. 41, pp. 101906, Oct 2014.

[22] C. T. Badea, M. Drangova, D. W. Holdsworth and G. A. Johnson, "In vivo small animal imaging using micro-CT and digital subtraction angiography," *Phys Med Biol*, vol. 53, R319-50, Oct 2008.

[23] J. M. Boone, O. Velazquez and S. R. Cherry, "Small-animal x-ray dose from micro-CT," *Molecular Imaging*, vol. 3, pp. 149-157, Jul 2004.

[24] S. R. Cherry, M. E. Phelps and J. A. Sorenson, *Physics in Nuclear Medicine*, 4th ed. Philadelphia, PA: Saunders, 2012, pp. 225-227.